Capturing the bursting dynamics of a two-cell inhibitory network using a one-dimensional map

Victor Matveev · Amitabha Bose · Farzan Nadim

Abstract Out-of-phase bursting is a functionally important behavior displayed by central pattern generators and other neural circuits. Understanding this complex activity requires the knowledge of the interplay between the intrinsic cell properties and the properties of synaptic coupling between the cells. Here we describe a simple method that allows us to investigate the existence and stability of anti-phase bursting solutions in a network of two spiking neurons, each possessing a T-type calcium current and coupled by reciprocal inhibition. We derive a one-dimensional map which fully characterizes the genesis and regulation of anti-phase bursting arising from the interaction of the T-current properties with the properties of synaptic inhibition. This map is the burst length return map formed as the composition of two distinct one-dimensional maps that are each regulated by a different set of model parameters. Although each map is constructed using the properties of a single isolated model neuron, the composition of the two maps accurately captures the behavior of the full network. We analyze the parameter sensitivity of these maps to determine the influence of both the intrinsic cell properties and the synaptic properties on the burst length, and to find the conditions under which multistability of several bursting solutions is achieved. Although the derivation of the map relies on a number of simplifying assumptions, we discuss how the principle features of this dimensional reduction method could be extended to more realistic model networks.

Keywords Half-center bursting ·
T-type calcium current · Poincaré return map ·
Multistability · Dimensional reduction

V. Matveev (✉) · A. Bose · F. Nadim
Department of Mathematical Sciences, New Jersey Institute
of Technology, Cullimore Hall, University Heights,
Newark, NJ 07102-1982, USA
e-mail: matveev@njit.edu

F. Nadim
Department of Biological Sciences, Rutgers University,
Newark, NJ 07102, USA

1 Introduction

Electrical bursting activity is a widely observed phenomenon in neurons and hormone secreting cells (Selverston and Moulins 1986; Bertram and Sherman 2000; Sohal and Huguenard 2001; Llinas and Steriade 2006). Considerable effort has been made to classify different types of bursting activity resulting in many detailed mathematical models (Izhikevich and Hoppensteadt 2004; Coombes and Bressloff 2005). Bursting activity often depends on properties of the networks in which these neurons lie. For example, bursting in reciprocally coupled inhibitory networks can arise from ionic currents that produce post-inhibitory rebound, such as the low-threshold transient calcium current, known as the T-current (Perkel and Mulloney 1974; Wang and Rinzel 1994; Huguenard 1996).

Reciprocally inhibitory networks are common circuit elements in many neuronal systems, from the mammalian neocortex and hippocampus to the invertebrate

central pattern generators, and play a crucial role in rhythmogenesis (Traub et al. 1996; Wang and Buzsaki 1996). Central pattern generators, in particular, make use of reciprocal inhibition between pairs of neurons or populations of neurons as a general mechanism for producing out-of-phase oscillations (Satterlie 1985; Marder and Calabrese 1996). Consequently, reciprocal inhibition has been the subject of many theoretical studies that have demonstrated the existence of a multitude of possible network behaviors arising through distinct mechanisms (Skinner et al. 1994; Van Vreeswijk et al. 1994; Wang and Rinzel 1994). In many cases, reciprocally inhibitory networks demonstrate dynamically complex outputs such as irregular oscillations or multistability of distinct modes of activity (Terman et al. 1998).

When considering networks or even pairs of reciprocally coupled neurons, the high dimensionality of the ensuing set of equations is often an obstacle in analyzing the dynamics of the system. Various methods such as averaging and singular perturbation theory have proved useful for reducing the dimensionality of larger systems of equations in a variety of network models (Butera 1998; Lee and Terman 1999; Medvedev 2005). These approaches involve tracking the behavior of a smaller number of variables in a phase space of lower dimension than the original system. An alternative approach has been to ignore certain state variables of the system, and instead track quantities that are experimentally and mathematically measurable. The inter-spike interval (ISI), the time between successive spikes of a neuron, is one such quantity and Ermentrout and Kopell (1998), for instance, use this approach to derive a one-dimensional map based on the ISI that they use to prove the existence and stability of synchronous spiking solutions in a hippocampal network.

We are interested in exploring the anti-phase bursting activity arising from the interplay between the low-threshold calcium T-current and synaptic inhibition in a reciprocally coupled network of two inhibitory neurons. In such a model, we observe that several stable bursting states may exist for the same set of parameters (Fig. 1). Each of these states has a different number of spikes per burst and thus different cycle periods. In this study, we provide an analytically and numerically tractable method for proving the existence and stability of these anti-phase bursts. This method exploits time-scale separations of variables to construct a one-dimensional Poincaré map whose fixed points correspond to periodic anti-phase solutions. The map is the burst length return map which tracks the length of a burst from one cycle to another, and, as such, does not

directly track the state variables of the governing set of equations. Interestingly, the construction of this map does not even require the coupled network. Instead, it is constructed as the composition of two different maps, each of which can be derived by studying the properties of a single uncoupled cell. By restricting the two maps to parameter ranges that are consistent with anti-phase bursts, we can use these single-cell maps to characterize the solutions of the coupled two-cell network.

A primary advantage of our approach is that we are able to pinpoint how certain key parameters of the model affect each of the single-cell maps which, in turn, affect both the existence and the stability of anti-phase solutions. In situations where this solution is unstable, the map is used to construct higher order periodic (or possibly chaotic) solutions. Thus, we show that a wide range of dynamic outputs of the reciprocally coupled network can be examined by analyzing the one-dimensional Poincaré map.
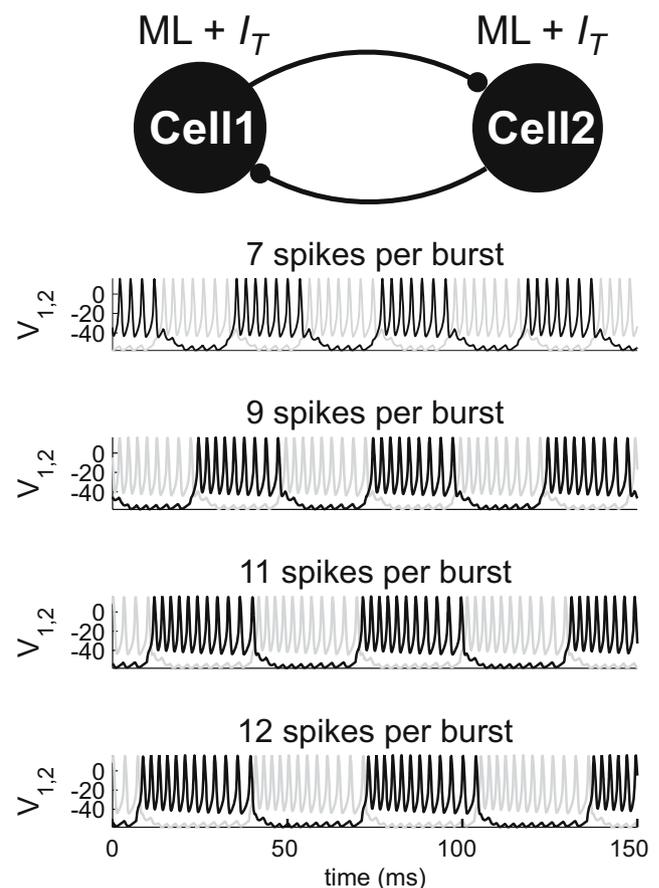

Fig. 1 A two-cell network of reciprocally inhibitory Morris–Lecar neurons with a T-current exhibits multiple stable periodic bursting solutions characterized by different number of spikes per burst for a single parameter set

2 Model

2.1 Single-cell dynamics

We first describe the dynamics of a single neuron. The two cells are assumed to be identical, each modeled as a two-variable Morris–Lecar oscillator (Morris and Lecar 1981), which we have modified to include a low-threshold Ca^{2+} current (T-current: I_T), described in detail further below. The spiking of the model cell results from the interplay between the dynamics of membrane potential v, and the recovery variable w, which describes the activation of the potassium current:

$$
\begin{cases}
C_m\, v' = I_{app} - g_L\,[v - E_L] - g_{Ca}\, m_\infty(v) \\
\qquad\quad [v - E_{Ca}] - g_K\, w\,[v - E_K] - I_T \\[4pt]
w' = \phi\, \dfrac{w_\infty(v) - w_K}{\tau_w(v)}
\end{cases}
\tag{1}
$$

where I_{app} is a constant applied current, g_L, g_{Ca} and g_K are conductances and E_L, E_{Ca} and E_K are reversal potentials for the leak, fast high-threshold calcium and potassium currents, respectively (Fig. 2). Both m_∞ and

(a)

(b)

Fig. 2 Single-cell dynamics: the Morris–Lecar oscillator (Eq. (1)) with $I_T = 0$. (**a**) In the absence of the T-current each uncoupled cell produces slow tonic spiking activity. (**b**) The phase-plane diagram demonstrates the periodic spiking arising from the interplay between the dynamics of the membrane potential v and the K^+ current activation variable w. The model parameters are chosen to produce Type-I excitability. The *dotted lines* shows the T-current inactivation threshold v_h

w_∞ are monotonically increasing sigmoidal functions of cell potential v. The functions and parameters are described in detail in Appendix 1.

The T-current in Eq. (1) models the low-threshold Ca^{2+} current with both activation and inactivation gating. Since the T-current activation is faster than its inactivation kinetics (Huguenard and McCormick 1992), we make the simplifying assumption that the activation variable is instantaneous and is described as a sigmoidal function of the membrane potential $a = a(v)$. The inactivation variable of the T-current is given by the dynamic variable h. For the mathematical analysis we make the further simplifying assumption that the activation function and the steady-state inactivation function are Heaviside functions of the membrane voltage. We discuss the implications of relaxing this assumption in the Discussion section. Also, the activation and steady-state inactivation curves are smoothed out to sigmoidal form in the simulations, as described in Appendix 1. The T-current is therefore described as

$$
I_T = \bar{g}_T a h [v - E_{Ca}]
\tag{2}
$$

$$
a = H(v - v_h)
\tag{3}
$$

$$
h' = \begin{cases}
(1 - h)/\tau_{lo} & v < v_h \\
-h/\tau_{hi} & v > v_h
\end{cases}
\tag{4}
$$

where $H(v)$ is the Heaviside function. The inactivation variable h decreases to zero if the cell is depolarized above v_h (*inactivation*), and increases to 1 if a cell is hyperpolarized below v_h (*de-inactivation*). We assume for simplicity that the T-current activation and inactivation thresholds are equal.

Our choice of model parameters corresponds to Type-I excitability (in the absence of synaptic coupling and the T-current): each cell spikes at a low baseline frequency, as shown in Fig. 2(a). The phase portrait of each cell in the absence of the T-current is illustrated in Fig. 2(b). The nullclines for Eq. (1) are obtained by setting the right-hand side equal to zero. When $I_T = 0$ the v-nullcline is cubic shaped, while the w-nullcline is sigmoidal (see Fig. 2(b).) Note that the T-current inactivation threshold v_h is chosen to be below the minimal value of v of the spiking trajectory of an uncoupled cell (Fig. 2). Therefore, the T-current is completely inactivated during tonic spiking ($h = 0$), and plays no role in the dynamics of the uncoupled cell.

The main effect of I_T is to produce a rebound burst of spikes in response to hyperpolarization, as shown in Fig. 3. If a hyperpolarizing current pulse lowers the cell potential below v_h (horizontal bar in Fig. 3(a)), then a gradual de-inactivation of the T-current occurs,
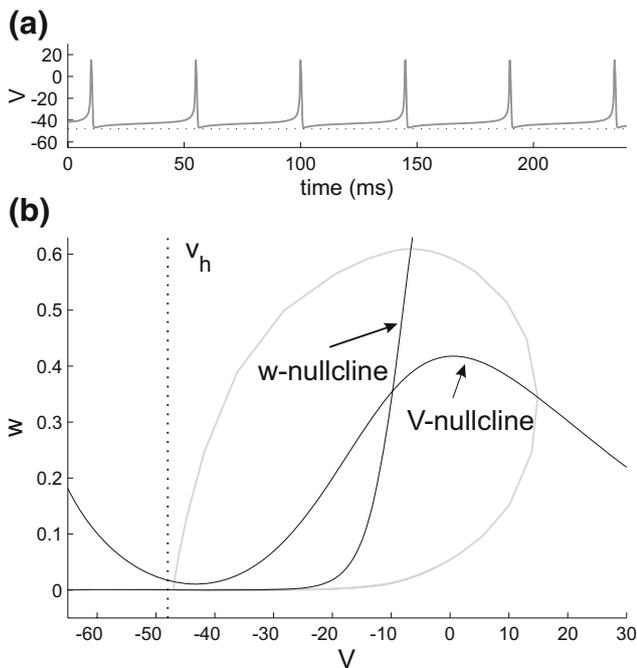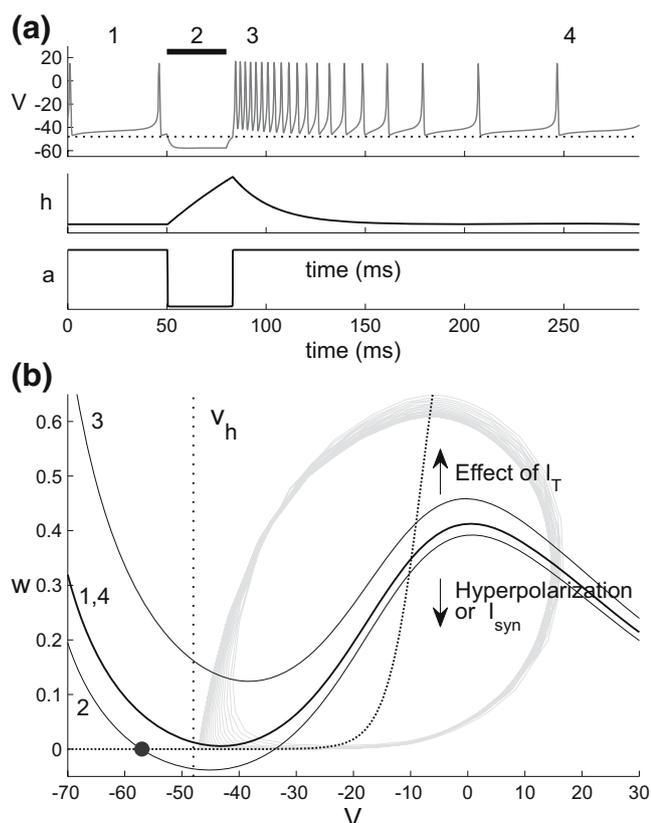
Fig. 3 Post-inhibitory rebound induced by the T-current. (**a**) Time course of cell potential (*top panel*), I_T inactivation h (*middle panel*), and I_T activation a (*bottom panel*), in response to a hyperpolarizing pulse (*horizontal bar*) applied during $t \in$ [50, 80] ms. Hyperpolarization pushes v below I_T inactivation threshold, v_h (*dotted line*), allowing I_T to de-inactivate (h grows). When hyperpolarization is removed, I_T is activated (*bottom panel*). The decrease in spike frequency during the rebound burst is caused by the decay of h (inactivation). (**b**) Effect of a hyperpolarizing pulse in the v-w phase plane. The positions on the v-nullcline labeled as 1, 2, 3 and 4 correspond to the accordingly labeled time points in (**a**). The hyperpolarizing pulse lowers the v-nullcline (2), creating a stable hyperpolarized equilibrium (*circle*). Note that the equilibrium lies to the *left* of v_h, allowing I_T to de-inactivate (h grows). When hyperpolarization is relieved, the v-nullcline shifts up (3), leading to a burst of action potentials (spike frequency is proportional to the elevation of the *left knee* of the v-nullcline). During the burst I_T gradually inactivates, and the nullcline goes back to its unperturbed location (1, 4). The trajectory of the rebound burst sweeps the *gray area*

i.e. h increases. When such external hyperpolarization is removed, the cell will depolarize above v_h, causing the activation of the T-current (a grows), which results in a burst of action potentials. In phase space, the activation of the T-current lifts the v-nullcline above its resting position, increasing the spike frequency due to larger distance of the periodic trajectory from the lower branch of the w-nullcline (Fig. 3(b)). During the rebound burst, the T-current gradually inactivates (h

decreases) with time constant of inactivation equal to τ_{hi} (see Eq. (4)). This inactivation manifests itself in the decrease of spike frequency during the burst. In phase space, inactivation corresponds to the gradual lowering of the v-nullcline (Fig. 3(b)), from the elevated position (labeled *3*) to the rest position (labeled *1, 4*).

2.2 Effect of synaptic inhibition

The network we consider includes two neurons described by Eqs. (1–4), reciprocally coupled by synaptic inhibition. The model for the synaptic current is adapted from Bose et al. (2001), and is given by ($i, j = 1, 2, i \neq j$):

$$I_{syn} = -\bar{g}_{syn} s_i [v_j - E_{inh}]$$

$$s_i' = \begin{cases} (1 - s_i)/\tau_g & v_i > v_\theta \\ -s_i/\tau_{syn} & v_i < v_\theta \end{cases} \tag{5}$$

where v_θ is the spike threshold that intersects the middle branch of the v-nullcline and s_i is the gating variable describing the synaptic input from neuron i to neuron j. The synaptic growth (onset) time constant is short compared to the spike width, thus allowing s_i to reach its maximal value with each action potential. We consider the case of intermediate to slow synaptic decay time, with τ_{syn} exceeding the spike width ($\tau_{syn} > \tau_w$). This results in the following full set of model equations ($i, j = 1, 2, i \neq j$):

$$C_m v_j' = I_{app} - I_L(v_j) - I_{Ca}(v_j)$$
$$- I_K(v_j, w_j) - I_T(v_j, a_j, h_j) - I_{syn}(s_i, v_j)$$

$$w_j' = \phi \, \frac{w_\infty(v_j) - w_K}{\tau_w(v_j)}$$

$$h_j' = \begin{cases} (1 - h_j)/\tau_{lo} & v_j < v_h \\ -h_j/\tau_{hi} & v_j > v_h \end{cases} \tag{6}$$

$$s_j' = \begin{cases} (1 - s_j)/\tau_g & v_j > v_\theta \\ -s_j/\tau_{syn} & v_j < v_\theta \end{cases}$$

$$a_j = H(v_j - v_h)$$

The influence of inhibitory synaptic input to a cell is opposite to that of the T-current. In the $v - w$ phase plane, the effect of inhibition from cell i to j is to lower the cubic shaped v-nullcline, which causes a decrease in the frequency of spiking. If inhibition is sufficiently weak (small $\bar{g}_{syn}$), both cells will continue spiking, and their spiking trajectories are only slightly perturbed by the coupling. In this case the inhibitory input is not enough to hyperpolarize the partner cell below

v_h, and therefore the T-current remains inactive and plays no role in cell dynamics. For stronger synaptic coupling strength $\bar{g}_{syn}$, however, a spike in one cell may be sufficient to hyperpolarize the other cell below its T-current de-inactivation threshold. In this case, the T-current will play a role in the network dynamics and, in particular, will make anti-phase bursting possible.

A quantity of central interest to us is the inter-spike interval (*ISI*). The *ISI* measures the time between successive spikes of the same neuron. We will use ISI_{tonic} to denote the inter-spike interval of the tonic spiking uncoupled cell. We choose parameters so that this value is relatively large, as compared to the shorter *ISI*s generated by the bursting mechanism described below.

3 Results

3.1 Half-center (anti-phase) bursting

The I_T-induced post-inhibitory rebound burst mechanism can work synergistically or cooperatively with the synaptic inhibition to entrain the network into a periodic anti-phase bursting state (Fig. 4; see Perkel and Mulloney 1974, Huguenard 1996, and Destexhe and Sejnowski 2003, for related work). This periodic bursting is a half-center oscillation where the two cells are active out of phase with one another (see Fig. 4(a)). The half-center oscillation requires a sufficiently strong synaptic coupling $\bar{g}_{syn}$, so that a burst of one cell (say, cell 1) provides enough synaptic current to hyperpolarize the postsynaptic cell (cell 2) below v_h, causing its T-current to gradually de-inactivate (h_2 grows). At the same time, the T-current of cell 1 gradually inactivates (h_1 decreases), and its *ISI*s grow larger, approaching the uncoupled cell's intrinsic spiking period, ISI_{tonic}. This increase in *ISI* eventually allows the inactive cell 2 to escape from inhibition. This happens when the inter-spike interval increases beyond a certain critical value, $\overline{ISI}$ (discussed in detail below). Once the suppressed cell escapes from inhibition, its potential increases beyond v_h. Since h_2 is now non-zero, the I_T current rapidly activates, producing a burst of spikes, terminating the burst of cell 1, and hyperpolarizing it below v_h. The process then repeats.

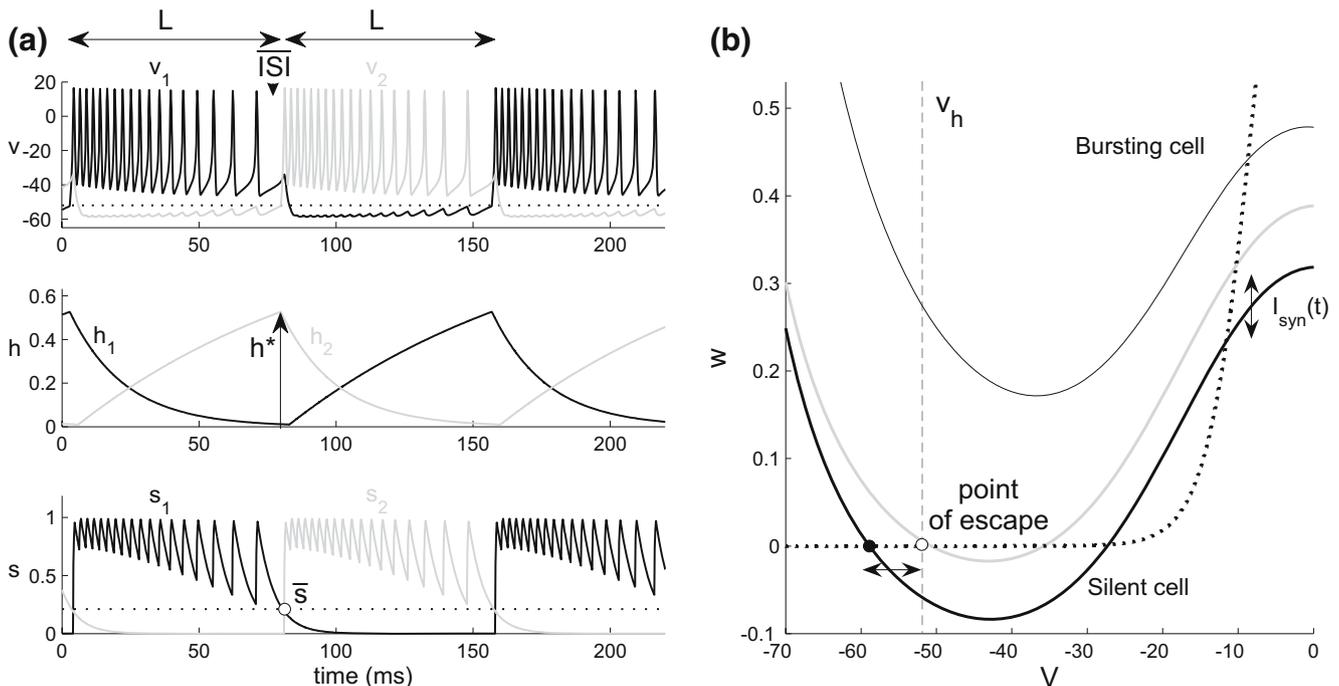The escape mechanism underlying the burst termination can be understood by considering the phase-

Fig. 4 Periodic anti-phase bursting of the coupled system of equations. (**a**) Time traces of the membrane potentials *(top panel)*, I_T inactivation, h_j *(middle panel)*, and the synaptic strength variables of the two cells, s_j *(bottom panel)*. (**b**) Phase plane dynamics of the network activity. The v-nullcline of the bursting cell gradually moves down as h decreases (inactivation).

The inhibitory synaptic input from the bursting cell lowers the v-nullcline of the postsynaptic cell, trapping the cell at an equilibrium *(filled circle)*. *Double arrows* indicate the oscillatory movement of the v-nullcline and the equilibrium point with each spike of the bursting cell. The *open circle* on the $v = v_h$ line marks the escape point of the suppressed cell (I_T activation threshold)

plane dynamics shown in Fig. 4(b). The v-nullcline of the bursting cell (*thin black* curve) is elevated, but gradually descends as I_T inactivates (h_1 decreases, *black* curve in middle panel of Fig. 4(a)), resulting in a gradual increase of the inter-spike interval for this cell (*black* curve v_1 in top panel of Fig. 4(a)). The inhibitory synaptic input from the bursting cell keeps the v-nullcline of the suppressed cell in a low position (*thick black* curve in (b)). Because of our assumption that $\tau_{syn} > \tau_w(v)$, the trajectory of the suppressed cell lies in a neighborhood of the intersection of the v and w-nullclines (*filled circle* in (b)). However, this intersection point moves left and right (double horizontal arrow in (b)) as the v-nullcline of the suppressed cell moves up and down with each spike of the bursting cell (double vertical arrow). The nullcline moves down quickly which each spike, and moves up somewhat slowly following the dynamics of the synaptic variable, $s_1(t)$, shown in the bottom panel of Fig. 4(a) (*black* curve). Accordingly, the membrane potential v_2 of the suppressed cell oscillates up and down (top panel in (a)), following this nullcline movement. As the *ISI* of the bursting cell increases, $s_1(t)$ decays to smaller and smaller values during the inter-spike interval, and the potential of suppressed cell moves closer to the T-current activation threshold (dotted vertical line, open circle in (b)). When the *ISI* is large enough to allow v_2 to reach v_h, the nullcline of the suppressed cell shifts up abruptly, due to the activation of its T-current, and the cell escapes from inhibition. The resulting burst of the previously suppressed cell terminates the burst of the active cell. The process then repeats with the two cells switching their roles.

The condition for escape of cell 2 can be described analytically by finding when it reaches the T-current activation threshold v_h. This occurs for a specific value of s, denoted $\bar{s}$, that satisfies:

$$I_{tot}(v_h, \bar{w}, \bar{s}) = 0$$
$$\bar{w} = w_\infty(v_h)$$

where $I_{tot} = I_{app} - I_L(v) - I_{Ca}(v) - I_K(v, w) - I_{syn}(v, s)$. Geometrically, this condition can be interpreted as the value of s at which the v- and w-nullclines intersect on the line $v = v_h$ (Fig. 4(b)). Solving for $\bar{s}$ and using the fact that $w_\infty(v_h) \approx 0$, we find

$$\bar{s} = \frac{I_{app} - g_L[v_h - E_L] - g_{Ca}m_\infty(v_h)[v_h - E_{Ca}]}{\bar{g}_{syn}[v_h - E_{inh}]} \quad (7)$$

This value $\bar{s}$ is closely related to the *ISI*. Namely, there exists a value $\overline{ISI}$ such that if $s(0) = 1$, then $s(\overline{ISI}) = \bar{s}$. Using Eq. (5), $\overline{ISI}$ satisfies:

$$\overline{ISI} = -\tau_{syn} \ln \bar{s} \quad (8)$$

Thus, $\overline{ISI}$ corresponds to the amount of time it takes a cell starting on the "$s = 1$" v-nullcline to reach the activation threshold v_h. Note that $\overline{ISI}$ is completely independent of the T-current properties since the suppressed cell feels no influence of I_T ($a = 0$ for $v < v_h$).

We now quantify the definition of bursting given earlier. We say that a cell is in the bursting regime if it exhibits a series of spikes for which the $ISI < \overline{ISI}$. Thus the term $\overline{ISI}$ allows us to use aspects of the nullcline geometry of the Morris–Lecar model to define the length of the burst.

3.2 The one-dimensional Poincaré map

The set of equations describing the dynamics of the two-cell network (Eq. (6)) forms a system of eight first order differential equations and two algebraic equations (for a_1 and a_2). Despite the high-dimensional phase space, it is possible to construct a one-dimensional Poincaré map which can predict the existence and stability of anti-phase burst states depicted in Fig. 1. The Poincaré map is the return map for the lengths of successive bursts and also determines the number of spikes per burst. It is constructed as the composition of two different single-cell maps. The first map, denoted $L = F(h^\star)$, determines the burst length of a cell as a function of $h^\star$, the level of T-current de-inactivation (h) at the beginning of the burst. The second map, denoted $h^\star = G(L)$ determines the amount of T-current de-inactivation as a function of the inter-burst length. We then define the return map $\mathcal{P}(L)$ by the relationship:

$$\mathcal{P}(L) = F(G(L))$$

We will show that a fixed point of this map corresponds to an anti-phase bursting solution for the coupled network given by Eq. (6). Both of the maps $F(h^\star)$ and $G(L)$ are constructed using information obtained from the dynamics of a single cell, coupled with restrictions imposed by the geometry of our model and by the condition of existence of a periodic half-center oscillation.

3.2.1 Dependence of burst length on the $h^\star$ value: $L = F(h^\star)$

To reconstruct the relationship $L = F(h^\star)$ between the burst length and $h^\star$, the level of T-current de-inactivation at the beginning of the burst, we study a single uncoupled cell. Suppose that at $t = 0$ the cell begins a burst with $h(0) = h^\star$. We will find the duration of each inter-spike interval ISI_n for a given value of $h^\star$, and then sum them up to obtain the burst length. Note that the length of each ISI_n is uniquely determined by
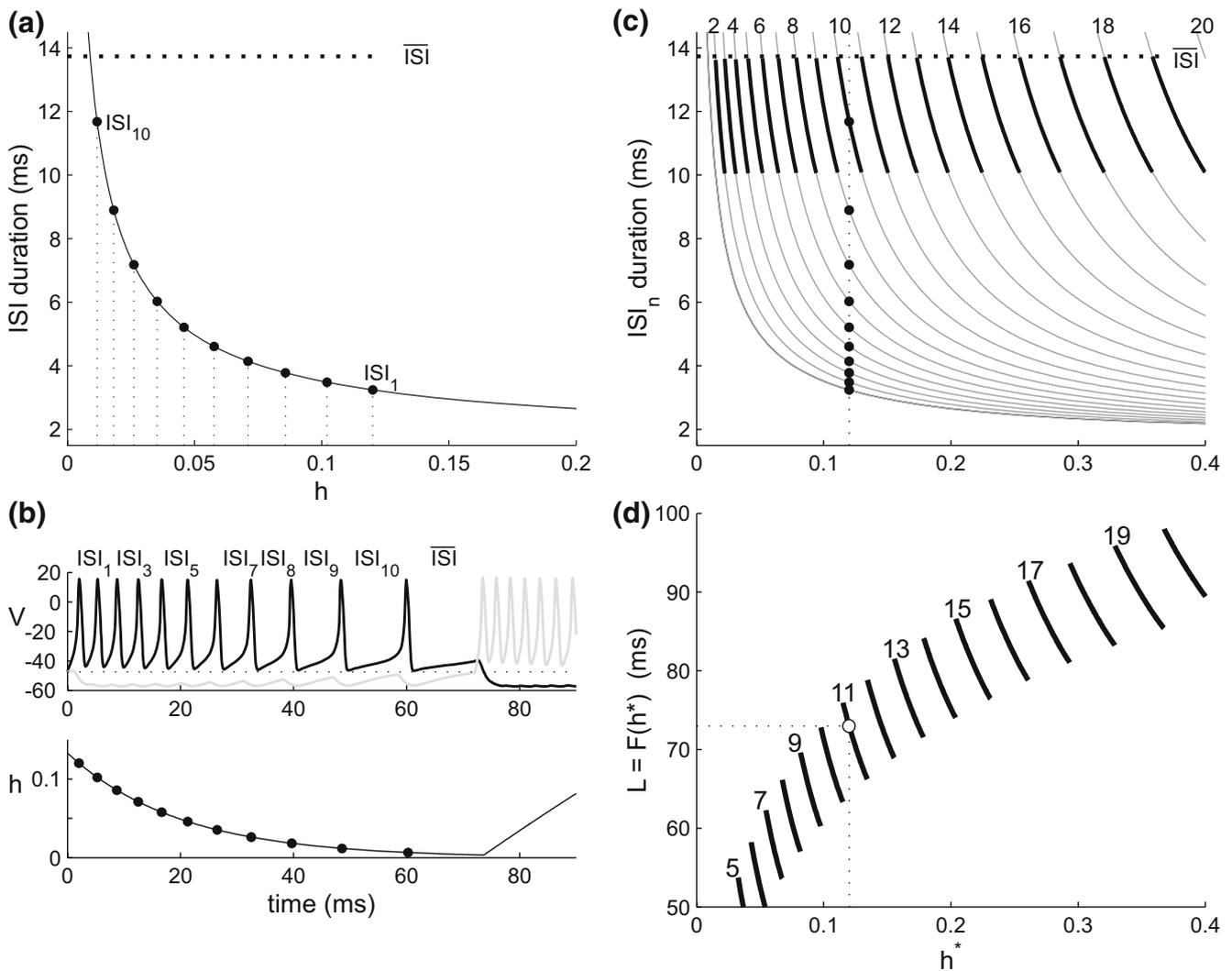
Fig. 5 Dependence of burst length on h, the level of T-current de-inactivation. (**a**) The relationship $T(h)$ between ISI and h in a single cell. *Filled circles* mark the values of h and the corresponding ISIs for a burst characterized by the initial condition $h(0) \equiv h^\star = 0.12$, and shown in panel (**b**). (**b**) Membrane potential (*top panel*) and T-current inactivation level h (*bottom panel*) for a numerically-generated burst with $h(0) = 0.12$ shown for illustrative purposes. *Filled circles* label the value of h at the beginning of each of the 10 inter-spike intervals (cf. (**a**)). (**c**) Dependence of each inter-spike interval on $h^\star$, the value of h at

the start of the burst. Each curve was generated using the $T(h)$ curve in panel (**a**) and Eqs. (9–10). Note that ISI_1 is the curve $T(h)$ shown in panel (**a**). The *horizontal dotted line* denotes $\overline{ISI}$. The *highlighted section* of each curve indicates the last ISI at a given value of $h^\star$. The *vertical dotted line* corresponds to the burst in panel (**b**). (**d**) The dependence of burst length on $h^\star$ is obtained by adding all ISI_n in panel (**c**) at each value of $h^\star$, plus $\overline{ISI}$. In (**c**), *numeric labels* indicate the index of last ISI in the burst, while in (**d**), the *integers* indicate the number of spikes per burst

the value of $h(t)$ right before the corresponding interval, h_n. This relationship is the same for all ISI_n's, and is given by a monotone decreasing function $ISI = T(h)$ as shown in Fig. 5(a). This curve may be thought of as a special version of the f-I curve of the cell, capturing the dependence of spiking period $ISI = 1/f$ on the level of depolarization provided by the T-current, which is proportional to h. The value $ISI_1 = T(h^\star)$ yields the length of the first inter-spike interval. The value of h at the beginning of the second interval, h_2, is determined

by the inactivation kinetics of h (see Eq. (4)): $h_2 = h^\star \exp\{-ISI_1/\tau_{hi}\}$). Since h_2 is smaller than $h_1 \equiv h^\star$, the second inter-spike interval, $ISI_2 = T(h_2)$, is greater than the first. Subsequent ISIs are obtained similarly. Thus:

$$ISI_n = T(h_n)$$
$$h_n = h_{n-1} \exp\{-ISI_{n-1}/\tau_{hi}\}$$
$$h_1 \equiv h^\star \tag{9}$$

The pairs (h_n, ISI_n) are labeled along the curve $T(h)$ in Fig. 5(a), for the particular case $h^\star = 0.12$, corresponding to the numerical simulation shown in Fig. 5(b).

It is useful to represent the duration of each ISI_n within a burst as a function of h at the very beginning of the burst, $h^\star$. As Eq. (9) illustrates, the dependence of each of the ISI_n intervals on $h^\star$ is governed by the same $T(h^\star)$ curve that determines ISI_1. Therefore for $n > 1$,

$$ISI_n(h^\star) = T(h_n) = T\big(h^\star \exp\big\{ - [ISI_1(h^\star) + ISI_2(h^\star)$$
$$+ ... + ISI_{n-1}(h^\star)]/\tau_{hi}\big\}\big) \qquad (10)$$

The $ISI_n(h^\star)$ curves are plotted in Fig. 5(c). The section of each curve highlighted in bold shows the last inter-spike interval of the burst for a given value of $h^\star$ (in Fig. 5(b), the last ISI_n is ISI_{10}). The vertical dotted line corresponds to the burst shown in panel (b). Note that each curve in the panel is obtained by stretching the curve $T(h)$ in panel (a) to the right, as described by Eq. (10).

To determine the burst length for any particular value of $h^\star$ we first sum all ISI_n values that lie below the critical value $\overline{ISI}$ (horizontal dotted line in Fig. 5(c)). Recall that the critical value $\overline{ISI}$ is determined by Eq. (8) and is used to indicate the termination of a burst. To complete the definition of $F(h^\star)$, we use the fact that, in half-center oscillations, exactly one cell is active at any time. Thus, $\overline{ISI}$ needs to be added to the sum of the ISIs to calculate the time from the last spike of one cell to the first spike of the other (see Fig. 5(b)). Therefore,

$$L = F(h^\star) = \sum_{j=1}^{n} ISI_j(h^\star) + \overline{ISI}, \; ISI_j < \overline{ISI}, \; j = 1..n \quad (11)$$

The function $F(h^\star)$, shown in Fig. 5(d), has two important features. First, it is piecewise continuous, and second, it is decreasing on the subintervals where it is continuous. The latter observation is easy to understand since the original ISI vs. $h^\star$ curve is itself monotone decreasing. The function $F(h^\star)$ is discontinuous because as $h^\star$ is increased, new spikes are added to the burst at certain values of $h^\star$ denoted h_{cr_j}. In fact, h_{cr_j} are the values of h at which the ISI_j curves intersect the $\overline{ISI}$ line. As $h^\star$ increases through each value h_{cr_j}, the inter-spike interval ISI_j satisfies $ISI_j < \overline{ISI}$, resulting in the addition of another spike. For example, in Fig. 5(c), the vertical line at $h^\star = 0.12$ shows that the associated burst has 11 spikes and 10 ISIs. Thus the length of the burst in this case is given by

$$L = \sum_{j=1}^{10} ISI_j + \overline{ISI}.$$

If we were to increase $h^\star$ to the value 0.15, then the vertical line $h^\star = 0.15$ would intersect the curve ISI_{11} at a value smaller than $\overline{ISI}$. Therefore a new spike would be added to the burst since $ISI_{11} < \overline{ISI}$. The new burst length would be

$$L = \sum_{j=1}^{11} ISI_j + \overline{ISI} \qquad (12)$$

The size of the jump discontinuity in the burst length at each h_{cr_j} equals the length of the added inter-spike interval, $ISI_j(h_{cr_j}) = \overline{ISI}$.

Since the monotonic decay of the continuous stretches of $F(h^\star)$ reflects the monotonic increase in spike frequency with increasing $h^\star$, the rate of this decay is proportional to the value of conductance $\bar{g}_T$, which multiplies h in the expression for the I_T (Eq. (2)). In fact, the effect of the variation of the $\bar{g}_T$ parameter can be obtained by re-scaling the $h^\star$ axis in Fig. 5(c,d) (see Fig. 7(a) and discussion below). The value of the inactivation time constant τ_{hi} affects the slope and the magnitude of $F(h^\star)$ in a similar manner. Increasing τ_{hi} slows down the T-current inactivation, decreasing the difference between successive ISIs shown in Fig. 5(a–b), and thereby increasing the number of ISIs that fit below the $\overline{ISI}$ burst termination limit for any given value of $h^\star$. This corresponds to the leftward "squeeze" of the $ISI_n(h^\star)$ curves in Fig. 5(c) toward the $ISI_1(h^\star)$ curve, thereby increasing the magnitude of $F(h^\star)$ by increasing the number of spikes per burst.

In contrast, as discussed above, $\overline{ISI}$ is only sensitive to the fast spike kinetics and the synaptic coupling parameters, and does not depend on the characteristics of the T-current. However, an increase in $\overline{ISI}$ would have a similar effect to an increase in τ_{hi}. Namely, it would increase the number of spikes per burst, and also increase the slope of the continuous stretches of $F(h^\star)$. In turn, an increase in $\bar{g}_{syn}$ or the membrane time constant would also influence $F(h^\star)$ through the effect of these parameters on $\overline{ISI}$.

Note that our method for constructing the $F(h^\star)$ easily generalizes to any model of single-cell dynamics, as long as each neuron has a well-defined $f - I$ curve, and all intrinsic currents except the T-current are fast compared to the time scales of synaptic inhibition and the T-current inactivation and de-inactivation. The specifics of the single-cell model would only affect the $T(h)$ curve in Fig. 5(a,c), while the value of $\overline{ISI}$ can always be determined numerically even if the analytical approximation given by Eqs. (7, 8) does not apply.
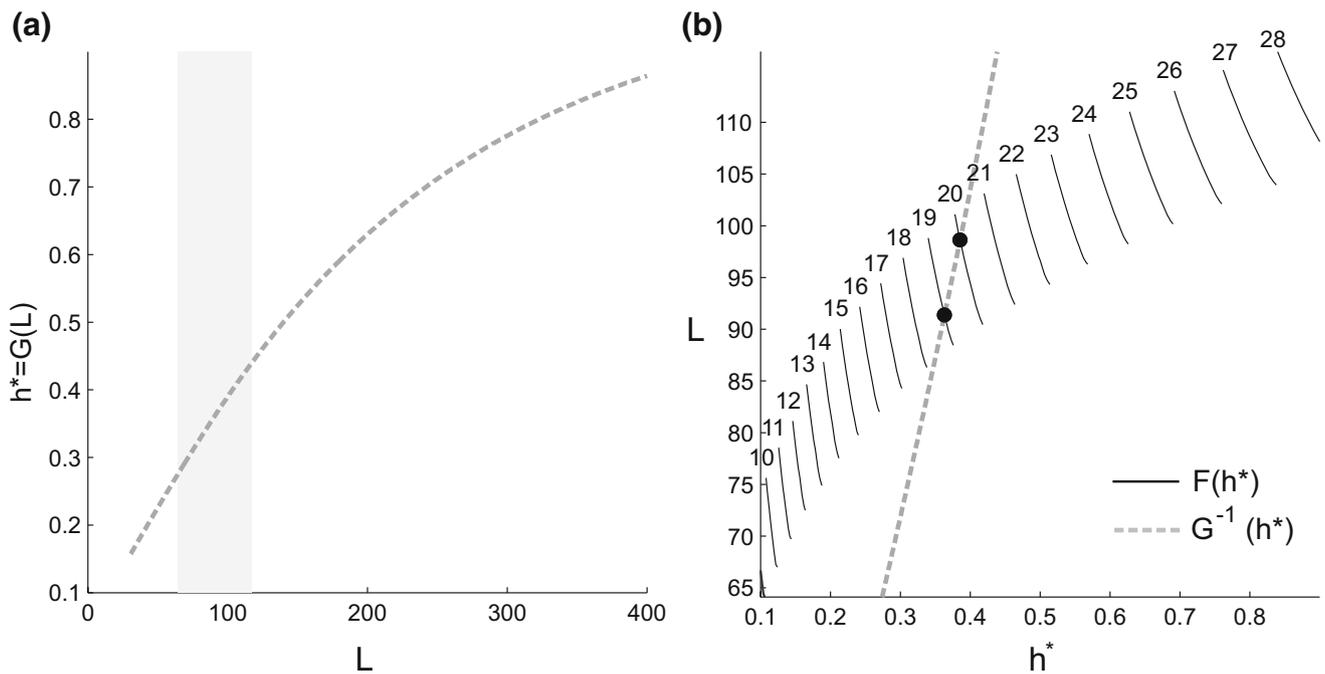
(a)

(b)

Fig. 6 The function $h^\star = G(L)$ obtained from Eq. (15) (**a**) and the fixed points of the Poincaré return map (**b**). (**a**) The dependence of $h^\star$, the I_T inactivation level at burst initiation, on the length of the preceding inter-burst interval, L, with $\tau_{lo} = 200$ ms and $\tau_{hi} = 20$ ms. The *gray box* corresponds to the axis limits in panel (**b**). (**b**) The stable periodic bursting solutions are obtained as the intersections of the piece-wise continuous

$L = F(h^\star)$ map see Fig. 5(d), and the inverse of the map shown in panel (**a**), $L = G^{-1}(h^\star)$ (*dashed curve*). The intersection points of the two curves correspond to the two stable periodic solutions, with 19 and 20 spikes per burst, respectively. Note that panel (**b**) implicitly describes the Poincaré return map, which is given by $\mathcal{P}(L) = F(G(L))$

3.2.2 Dependence of $h^\star$ on the burst length: $h^\star = G(L)$

The second part of Poincaré map, the dependence $h^\star = G(L)$ (see Fig. 6(a)) is easier to construct. It measures how the T-current of an uncoupled cell de-inactivates when the cell is silent. It follows straightforwardly from the first-order kinetics of the T-current de-inactivation given by Eq. (4):

$$\frac{dh}{dt} = \frac{1-h}{\tau_{lo}} \quad \text{when} \quad v < v_h$$

Solving this equation with $h(0) = h_o$ yields:

$$h(t, h_o) = 1 - (1 - h_o)e^{-t/\tau_{lo}}. \tag{13}$$

The value h_o is the minimum value of h obtained at the end of the burst (see Fig. 4). However, in the coupled network, there is no *a priori* way to know the value of h_o. Nonetheless, this value will be bounded from above by $\overline{h}$, defined as the value of $h^\star$ at the intersection of ISI_1 and $\overline{ISI}$, and bounded from below by $\overline{h} \exp(-\overline{ISI}/\tau_{hi})$. For definiteness, let $h_o = \overline{h}$. Evaluating Eq. (13) at $t = L$, we obtain:

$$h^\star = G(L) \equiv h(L, \overline{h}) = 1 - (1 - \overline{h}) \exp(-L/\tau_{lo}) \tag{14}$$

We note that for a periodic solution, we can replace $\overline{h}$ with its equilibrium value, $\overline{h} = h^\star \exp(-L/\tau_{hi})$. This yields an equilibrium condition for Eq. (14):

$$h^\star = G(L) = \frac{1 - \exp(-L/\tau_{lo})}{1 - \exp(-L/\tau_{lo} - L/\tau_{hi})} \tag{15}$$

The map $h^\star = G(L)$ is plotted in Fig. 6(a) using Eq. (15). Note that this map is only a function of the inactivation and de-inactivation time constants of the T-current, τ_{hi} and τ_{lo}, with a much greater sensitivity to τ_{lo} than to τ_{hi} (assuming $\tau_{hi} << \tau_{lo}$). Thus, the two maps $h^\star = G(L)$ and $L = F(h^\star)$ are controlled by two distinct sets of model parameters. As will be shown below, this fact greatly simplifies the understanding of the parameter control of the network's bursting dynamics.

3.2.3 Fixed points of the Poincaré map: $\mathcal{P} = F(G(L))$

Periodic solutions of Eq. (6) correspond to the fixed points of the Poincaré map $L_{eq} = \mathcal{P}(L_{eq}) \equiv F(G(L_{eq}))$. Introducing an equilibrium value of $h^\star$, $h^\star_{eq} = G(L_{eq})$, this equilibrium condition can also be written as $L_{eq} = F(h^\star_{eq}) = G^{-1}(h^\star_{eq})$. Therefore, geometrically the periodic solutions correspond to the intersections of the

graph of $L = F(h^\star)$, given in Fig. 5(d), and the inverse of the map $G(L)$ given by Eq. (15) and shown in Fig. 6(a). In Fig. 6(b) we superimpose these two maps and show their intersection points. Interestingly, the two curves share more than one intersection point, demonstrating that multiple bursting solutions can exist for the same parameter values. Indeed, below we verify numerically the existence of such multiple bursting solutions.

Apart from providing the information about the periodic network activity, the Poincaré map simplifies the parameter sensitivity analysis of the model, illustrating the control of the burst duration by various model parameters. This is achieved by examining the influence of model parameters on the two individual parts of the Poincaré map, the curves $F(h^\star)$ and $G(L)$. Consider for example the effect of a variation of $\bar{g}_T$, the maximal I_T conductance. As discussed above, $G(L)$ (Eq. (15)) is dependent on τ_{hi} and τ_{lo}, but is not sensitive to $\bar{g}_T$. The dependence on $\bar{g}_T$ of $F(h^\star)$ is straightforward: namely, an increase in $\bar{g}_T$ "squeezes" the $L = F(h^\star)$ curve to the left ($h^\star$ axis scales down with $\bar{g}_T$), as shown in Fig. 7(a). As a result, as $\bar{g}_T$ is increased, the Poincaré map intersections shown in Fig. 6(b) would lie along the segments of $F(h^\star)$ with larger number of spikes per burst.

In contrast, varying τ_{lo} affects only $G(L)$ and not $F(h^\star)$ (Fig. 7(b)). The change in $G(L)$ occurs because an increase in τ_{lo} effectively moves the G curve up (the L axis scales up with τ_{lo}). Thus, by changing different model parameters, different components of the Poincaré map are affected, leading to multiple degrees of control of the existence of periodic bursting solutions.

3.2.4 Stability of periodic bursting solutions

The stability of the periodic bursting solutions can be determined by checking the slopes of the graphs $L = F(h^\star)$ and $L = G^{-1}(h^\star)$ at a point of intersection. A burst solution will be stable if $|d\mathcal{P}/dL|_{L_{eq}} < 1$. This derivative satisfies

$$\left.\frac{d\mathcal{P}}{dL}\right|_{L_{eq}} = \left.\frac{dF}{dh^\star}\right|_{h^\star_{eq}} \left.\frac{dG}{dL}\right|_{L_{eq}} \tag{16}$$

The derivative dG/dL is easy to calculate from Eq. (14):

$$\frac{dG}{dL} = \frac{(1 - \bar{h})\exp(-L/\tau_{lo})}{\tau_{lo}}$$
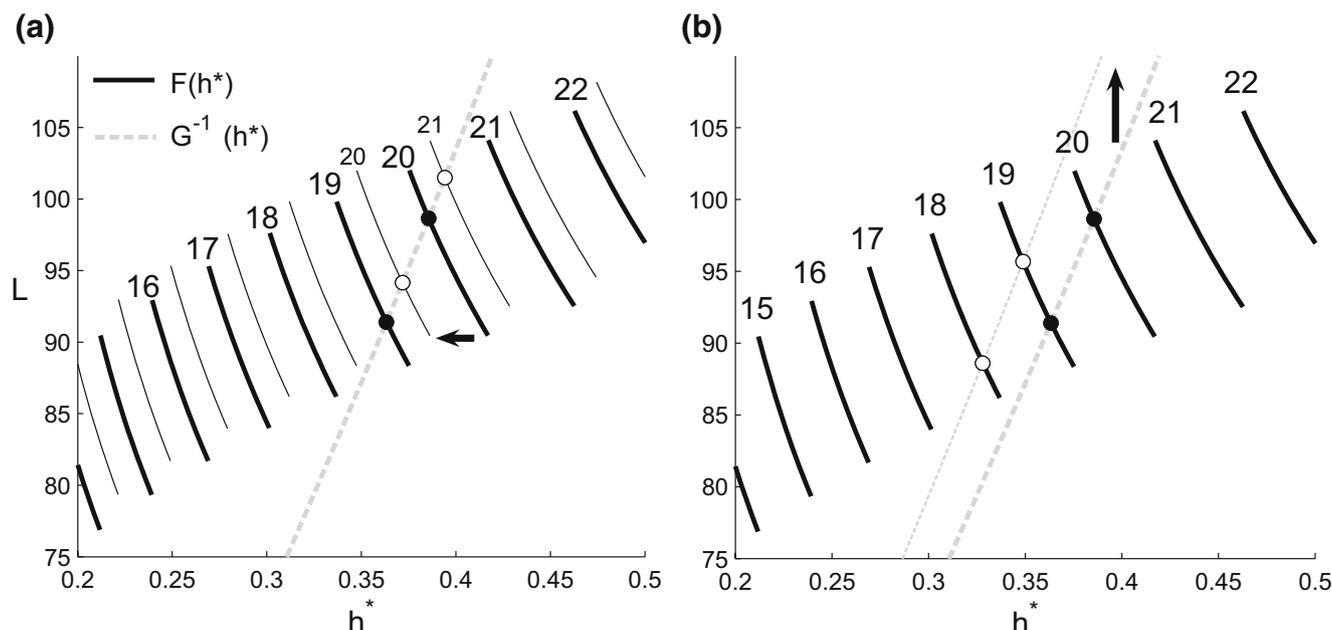

Fig. 7 Control of burst properties by parameters $\bar{g}_T$ and τ_{lo}. (**a**) An increase in the value of $\bar{g}_T$ from 1.0 to 1.08 mS/cm^2 is equivalent to a *horizontal contraction* of the $F(h^\star)$ map, but does not affect the $G(L)$ map. *Filled circles* indicate the stable periodic solutions for the parameter values corresponding to Fig. 6; *open circles* label the stable periodic solutions after the value of $\bar{g}_T$ is

increased from 1.0 to 1.08 mS/cm^2. Note that the bursting state with 19 spikes per burst disappears and is replaced by a solution with 21 spikes per burst. (**b**) An increase in the value of τ_{lo} from 200 to 220 ms causes a *vertical stretch* of the $G(L)$ map, but has no effect on the $F(h^\star)$ map. Note that the bursting solution with 20 spikes is replaced with a solution with 18 spikes per burst

which clearly shows dependence on the parameter τ_{lo}. It is also indirectly affected by other parameters such as τ_{syn} since this synaptic time constant affects $\overline{ISI}$ and hence $\overline{h}$. The derivative $dF/dh^\star$ is harder to explicitly quantify. Note, however, that since each inter-spike interval in the burst is inversely proportional to h, each spike contributes to the slope of the $F(h^\star)$ curve. Therefore, the relationship between L and $h^\star$ becomes progressively more steep at higher values of τ_{hi}. Likewise, the derivative $dF/dh^\star$ grows with increasing $\bar{g}_T$ since this parameter increases the number of spikes per burst as well.

It is straightforward to numerically calculate the value of $dF/dh^\star$ at a point of intersection. This is what we did, for example, in Fig. 6(b) to conclude the stability of the obtained solutions. We further tested how well the Poincaré map, based on single cell dynamics, correctly determines the dynamics of the coupled network by numerically solving the latter. Figure 8 shows the numerically reconstructed phase diagram of the model network, indicating the stable periodic activity states as a function of the I_T conductance, $\bar{g}_T$ (see Appendix 2 for details of the numerical crawl algorithm used to construct the phase diagram). Note the overlap between the regions of stability of the various bursting solutions, in agreement with the multistability exhibited by the Poincaré map in Fig. 6(b). The phase diagram also validates the dependence of burst length on the value of $\bar{g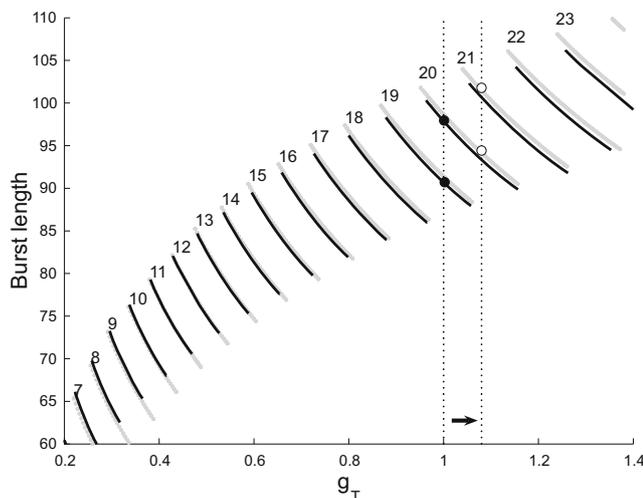}_T$ inferred above by analyzing the Poincaré return map (Fig. 7). Namely, it shows that an increase in $\bar{g}_T$ increases the number of spikes per burst. Note that a more dramatic increase in $\bar{g}_T$ would also reduce the number of co-stable bursting solutions (cf. Fig. 11).

The analysis above suggests that the parameters τ_{hi}, τ_{lo}, $\bar{g}_T$ and τ_{syn} affect both the existence and the stability of periodic solutions. For example, the parameter variations shown in Fig. 7 changed the number of spikes per burst but preserved the stability of the equilibrium points, as determined from Eq. (16). However, a more drastic increase in $\bar{g}_T$ or a decrease in τ_{lo} can change the slopes of the corresponding parts of the Poincaré map to the extent that the equilibrium points become unstable.

The loss of stability can be also achieved by increasing the value of τ_{syn}, as is shown in Fig. 9(a). According to Eq. (8), increasing τ_{syn} increases $\overline{ISI}$. With our choice of parameters, the value $\overline{ISI}$ intersects the curve $T(h)$ along a very steep portion of this curve (Fig. 5). Thus an increase in $\overline{ISI}$ can change the burst length quite significantly, but not change the corresponding h value much. Thus the slope of the function $F(h^\star)$ is quite sensitive to changes in $\overline{ISI}$. Figure 9(b,c) demonstrates this fact and shows the dynamics of the network for $\tau_{syn} = 10$ ms for which no stable periodic solution exists.

3.2.5 Relaxing some assumptions leads to greater multistability

The analysis presented above relies on a number of assumptions. Notably, we assumed that synaptic decay is faster than spiking dynamics, which allowed us to formulate the escape condition in terms of the critical value of $\overline{ISI}$ (Eq. (8)). Further, we assumed that v_h lies just below the spiking threshold of each cell. This ensures that the bursting cell falls below the T-current (de-)inactivation threshold immediately after its burst is terminated by the escaping cell, leading to exact anti-phase solutions demonstrated in Figs. 2–7.

Figure 10 shows that the above constraints may be relaxed without loss of the qualitative features of the Poincaré map. In this figure the value of v_h has been lowered from -47.5 to -52 mV, and the synaptic decay time is 1 ms. The time trace in panel (a) shows that there is a significant lag (labeled ϕ) between the escape time of one cell and the time that the inhibition pushes the other cell below the T-current threshold. The main result of this lag is a shift in the value of h at the transition to the silent state, i.e. when v drops below v_h. Thus we can no longer utilize Eqs. (14) or (15) to calculate
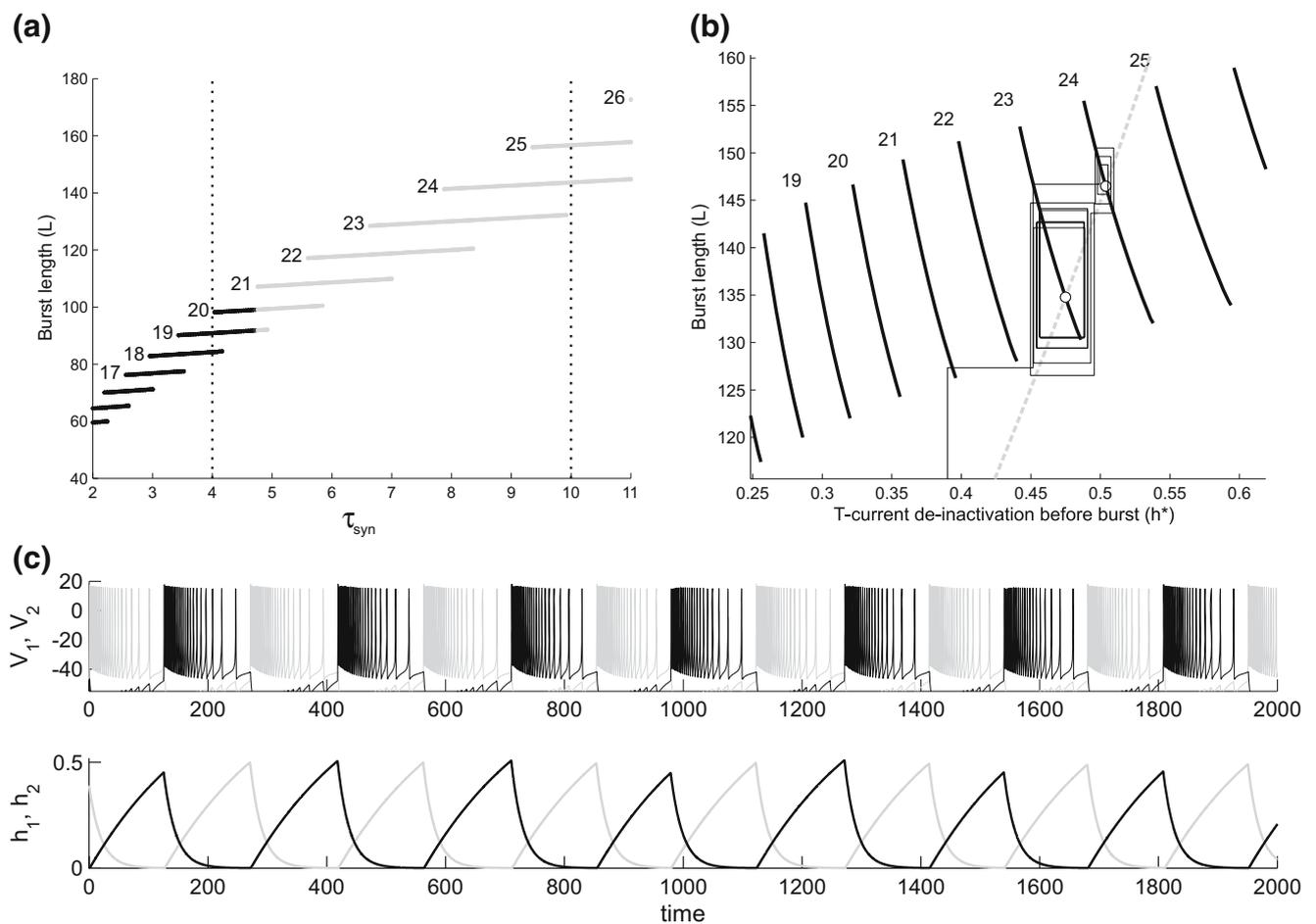

Fig. 8 Comparison of the bifurcation diagrams for the bursting states as a function of T-current conductance, obtained from the Poincaré map (*black*) and by the numerical crawl algorithm (*gray*). The *dashed lines and circles* mark the values $\bar{g}_T = 1.0$ and $\bar{g}_T = 1.08$ mS/cm^2 and the corresponding stationary states shown in Fig. 7(a)

Fig. 9 Dynamics of the network near unstable equilibria. (**a**) Bifurcation diagram as a function of the synaptic decay time constant τ_{syn} obtained from the single-cell map $L = F(h^\star)$. *Black curves* label the stable periodic solutions, while the *gray curves* label the unstable solutions. Note that the stability of periodic bursting is lost near $\tau_{syn} = 4.8$ ms. The *dashed lines* mark the value $\tau_{syn} = 4$ ms corresponding to Figs. 4–8 and the value

$\tau_{syn} = 10$ ms corresponding to panel (**b**). (**b**) The dynamics of the network for $\tau_{syn} = 10$ ms, shown as a cobweb and obtained by parsing the numerically integrated solution to the network equations, shown in panel (**c**). Note the irregular pattern of the peak value of T-current de-inactivation (h^*) apparent in the time trace shown in (**c**), corresponding to the (possibly) chaotic dynamics of the discrete Poincaré map shown in (**b**)

the map $h^\star = G(L)$. Instead, we numerically calculate the map using a feed-forward network and the steady-state approximation. Namely, we consider a network in which cell 1 inhibits cell 2 with cell 1 starting in the bursting regime with $h = h^\star$ and cell 2 in the silent state with $h = h^\star \exp(-L/\tau_{hi}) \equiv h_L$. For different values of L for cell 1, we calculate the time $\phi(h^\star)$ before v_2 falls below v_h. This is done using simulations of the feed-forward network. We then use this information and the steady-state approximation to numerically and iteratively solve for the function $h^\star = G(L)$. The inverse of the function $h^\star = G(L)$ is plotted in Fig. 10(b). Note that this map has a number of discontinuities that arise at values of L below which an extra spike is required to inhibit the suppressed cell below v_h (see Appendix 3 for more details). Interestingly, in this case, the discontinuity increases the number of stable periodic solutions

that exist. As is shown, as many as six stable periodic bursting solutions exist, corresponding to the six points of intersection of the two maps, for the same values of parameters. Several of these solutions are shown in Fig. 1. Figure 11 shows the numerically-generated phase diagram obtained by using the crawler method (see Appendix 2) on the coupled network for the new parameter values. Note that multistability is achieved for a range of $\bar{g}_T$ values, which provides evidence that the Poincaré map formalism (this time partially based on a feed-forward map as opposed to a single-cell map) is valid. A qualitatively different case of multistability of periodic bursting states has been previously analyzed in the context of a single-cell bursting model of Canavier et al. (1991, 1994) by Butera (1998), using an approach which is very similar to the one adopted in this work (see below).
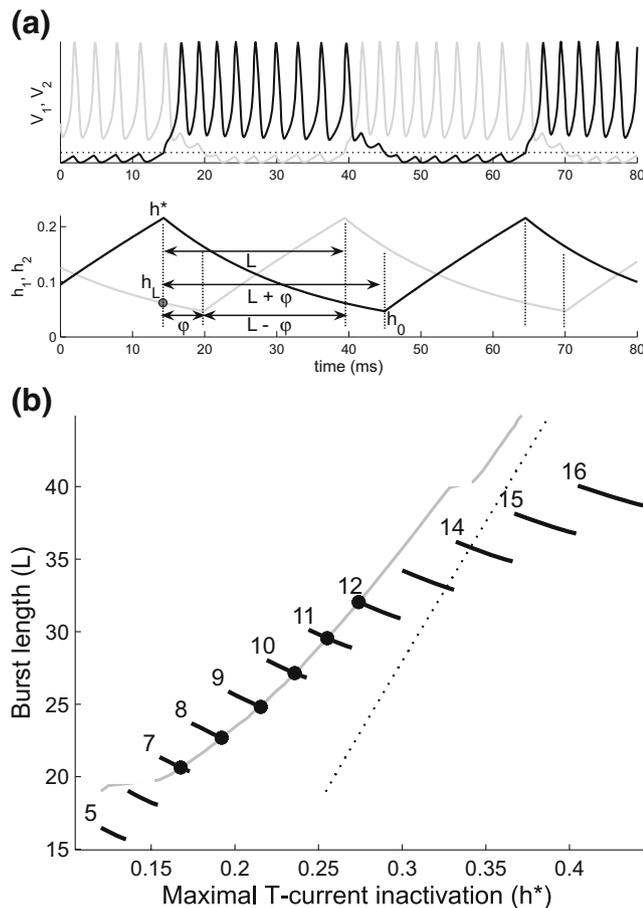
Fig. 10 Poincaré map for the case of faster synaptic decay ($\tau_{syn} = 1$ ms) and lower T-current activation/inactivation threshold ($v_h = -52$ mV). (**a**) shows the potential and T-current inactivation of the two cells for the nine spikes per burst solution (shown also in Fig. 1). Note that the T-current dynamics of the two cells are not completely anti-phase, due to the lag between cell escape time and the time of suppression of the other cell below v_h (ϕ, *double arrow*). (**b**) The Poincaré map. Note that the $G(L)$ map is discontinuous; each discontinuity corresponds to the value of L below which an extra spike is required to inhibit the suppressed cell below v_h (see Appendix 3). *Dashed line* corresponds to the $G(L)$ curve obtained under assumption of half-center bursting. Four of the six stable periodic bursting solutions are shown in Fig. 1(b)

4 Discussion

4.1 Summary

There have been countless biophysical models of neurons and networks in the past two decades that have successfully reproduced outputs of their biological counterparts and made numerous useful predictions (Hines et al. 2004). In almost every case the models themselves produce quite complex outputs which, due to the large number of parameters and variables in-

volved, are quite difficult to analyze. In the current study, we take one such model, a two-cell anti-phase half center oscillator producing bursting activity, and analyze it by focusing on outputs of interest and reducing the original system of differential equations to a one-dimensional map. We then show that the analysis of the one-dimensional map provides information about both existence and stability of solutions to the original high-dimensional system.

We studied a network of two identical neurons coupled with reciprocally inhibitory synapses. Each neuron was constructed as a Morris–Lecar model to produce the spiking activity together with a low-threshold calcium (T-type) current. The synapses are action-potential mediated with fast rise and intermediate decay time constants. We described an analytic method that produces a Poincaré return map formed as the composition of two one-dimensional maps (F and G) of an interval. Each of these maps is constructed by using the properties of a single isolated neuron: the map G yields the level of inactivation/de-inactivation (h^*) of the T-current at the transition to bursting as a function of the time interval during which the cell is inactive; the map F produces the burst duration L as a function of h^*. These two maps depend on different sets of model parameters.

4.2 Significance

There is a large body of literature on reciprocally coupled inhibitory networks. These networks arise naturally in central pattern generating circuits that control rhythmic motor activity (Perkel and Mulloney 1974; Marder and Calabrese 1996; Grillner et al. 2005). In such networks, anti-phase bursting outputs of neurons is ubiquitous and results in the out-of-phase activity of opposing groups of muscles such as flexors and extensors. Inhibitory networks have also been studied in the context of synchronization, especially in the presence of slowly decaying synapses (Wang and Rinzel 1992; Van Vreeswijk et al. 1994; Terman et al. 1998). Our analysis only deals with anti-phase solutions and specifically omits the analysis of synchrony.

Post-inhibitory rebound in networks with T-currents has also been studied quite extensively (Wang and Rinzel 1994; Huguenard 1996; Destexhe and Sejnowski 2003). While our study fits in this context, our primary reason for including the T-current in our model was not to achieve post-inhibitory rebound—the model cells spike in the absence of input and thus do not need the rebound to fire—but rather to work cooperatively with the synapse to control the burst duration. The presence of the T-current enables the model to produce bursting
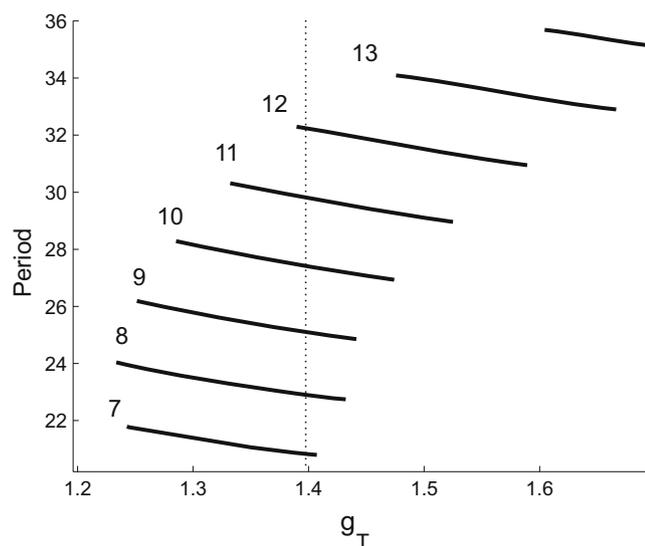
Fig. 11 Numerically reconstructed bifurcation diagram as a function of T-current conductance, $\bar{g}_T$, for the case of fast synaptic decay and low v_h. *Dotted line* corresponds to the value of $\bar{g}_T$ in Fig. (10)

activity with a large range of burst periods depending on the T-current parameters. In fact, the presence of the T-current is essential for multistability of solutions with different burst durations. However, our analysis would still apply if the bursting was due to the slowly-activating potassium current rather than the T-current.

The primary advantage of our method is that it provides a simple tool for the identification of parameters that control the existence and stability of the bursting solutions. For example, the map $h^\star = G(L)$ was shown to depend only on the T-current inactivation and de-inactivation time constants, while the map $L = F(h^\star)$ depended both on the T-current properties and the properties of the synapse. This analysis also enabled us to show how parameters of the synapse and of the T-current interact to determine the burst length and the number of spikes per burst. A second advantage of our method is that it reveals the circumstances under which single-cell or feed-forward maps—constructed by tracking a network quantity through a feed-forward subnetwork—can be used to characterize the dynamics of the coupled (feedback) network. For example, both the symmetric anti-phase bursting solutions and the more complex chaotic anti-phase bursting (see Fig. 9) are found as fixed points and chaotic trajectories of the one-dimensional map, respectively. Note that the maps constructed in our study are of lower dimension, and thus easier to analyze, than standard Poincaré return maps that track the state variables. Yet, we demonstrated that the one-dimensional map yields excellent qualitative and quantitative agreement with solutions

of the full network obtained by numerically solving the full set of equations (Figs. 8, 9(b); cf. Figs. 10(b) and 11).

Reduction to lower-dimensional maps to prove existence and stability of solutions has been used in a wide variety of contexts (Butera 1998; Lofaro and Kopell 1999; Lee and Terman 1999; Medvedev 2005; Terman 1994). Most of these studies involve tracking state-variables in a lower-dimensional phase space. For example, Terman et. al. have used geometric singular perturbation theory to derive low dimensional maps to find oscillatory solutions in a variety of networks (Rubin and Terman 2000; Terman 1994; Terman et al. 1998). Butera (1998) used a Poincaré return map to analyze the multistability of bursting solutions and chaotic bursting displayed by the *aplysia* bursting neuron model of Canavier et al. (1991, 1994). In each of these studies, a map, defined on a lower dimensional slow manifold, tracks a subset of the state variables of the full system. Medvedev has shown how to construct one-dimensional maps using singular perturbation theory and averaging to understand the complicated dynamics of a bursting neuron model of Chay (Chay and Rinzel 1985; Medvedev 2005). This method involves deriving a return map for the single slow variable of the model and understanding its bifurcation structure. A notable exception to tracking state variables can be found in the work of Ermentrout and Kopell (1998) in which the inter-spike interval (*ISI*) is tracked to construct a one-dimensional map associated with a hippocampal network. This map is formed as a combination of two feed-forward maps, similar in spirit to the two single-cell maps in our study. The map constructed by Ermentrout and Kopell tracks spikes of different cells in a four-cell network and shows that synchronization can be closely tied to the existence of a spike doublet from a specific cell in the network.

Our approach bears close resemblance to the above-mentioned work of Butera (1998), who obtained the return map capturing the multistable bursting of a model cell as a composition of two separate components representing the spiking and the silent states of the bursting cell, respectively, In both studies, the component related to the active phase is a piece-wise continuous map, with each branch corresponding to a continuum of states with an identical number of action potentials. Finally, as in our case, one of the crucial parameters of their model exerted its influence on only one of the two components of the map, allowing a simple description of the burst length control by this parameter.

One significant consequence of the analysis presented in this work is the demonstration of multiple fixed points corresponding to bursting solutions with

different numbers of spikes per burst. As shown in Figs. 6–11, the stability of multiple such fixed points can give rise to multistability of bursting activity (see Fig. 1). To our knowledge, this is the first modeling study that examines the possibility of emergence of such network multistability from the interplay between the synaptic interaction and the intrinsic cell dynamics. As discussed above, the existence of multiple stable bursting solutions has been previously considered in the context of intrinsic cell bursting (Canavier et al. 1991, 1994; Butera 1998); however, it has not been carefully examined experimentally. On the other hand, there are known examples of bistability (Lechner et al. 1996; Manor and Nadim 2001). It is intriguing to speculate whether multiple stable periodic states could coexist in biological networks, enabling the system to quickly switch between distinct activity states. However, the basin of attraction of the distinct bursting solutions may be too narrow for these states to be reliably sustained. In biological systems, multistability of bursting activity is much more likely to manifest itself as cycle to cycle variability in the number of spikes per burst due to noise and other extrinsic influences on the network. Such variability is in fact observed in many half-center oscillatory networks (Bartos et al. 1999; Masino and Calabrese 2002).

4.3 Relaxing the simplifying assumptions

In order to implement our map-based approach, we made a few simplifying assumptions. First, we assumed that the synaptic and recovery variables evolved slowly in the silent state compared to the voltage variable. This allowed us to slave the v variable to the dynamics of the w and s variables thus enabling us to determine the value $\bar{s}$ (see Eq. (7)). This multiple-time-scale assumption is critical for using our single-cell map approach, but is less important if we wish to derive the map by analyzing the feed-forward network. For example, when we relaxed the time-scale separation by changing τ_{syn} from 4 ms to 1 ms, thus allowing s to evolve more quickly in the silent state, we were still able to use a feed-forward map to determine $h^{\star} = G(L)$ (see Fig. 10 and Appendix 3), which enabled us to accurately predict the behavior of the full model.

In our analysis we assumed that the T-current activation threshold (v_a) and inactivation threshold (v_h) are equal. If we consider the case $v_a > v_h$, then the T-current would begin to inactivate while the neuron is still in the silent state. If the inactivation rate is too fast, the effect of the T-current may be lost before it is activated. However, even if the inactivation rate is not too fast, constructing a single-cell map for $h^{\star} = G(L)$ would not be possible since we would need to know how the silent cell responds to individual synaptic events. However, a feed-forward approach to construct the map similar to the fast τ_{syn} case would still be possible, provided that v lies below v_a in the silent state. In this case $\bar{s}$ would be computed from Eq. (7) using the value of v_a instead of v_h. Further, we used a Heaviside function to demarcate the inactivation and activation thresholds. These functions are smoothed out when performing numerical simulations. They could also be smoothed out in the analysis and would mostly affect how we calculate the map $h^{\star} = G(L)$. We would no longer be able to explicitly calculate $\bar{h}$, but would instead have to estimate it.

In this paper, the post-synaptic cell escapes from inhibition when it reaches the T-current activation threshold. With a change of parameters, it is possible for this cell to instead be released from inhibition. For example, suppose each cell has a stable rest state at a potential larger than the T-current activation threshold v_h, and that the synaptic decay constant is large relative to the intrinsic time constant τ_w. The difference in scales of the time constants would imply that the post-synaptic cell could not reach v_h while the pre-synaptic cell is still active. Once the pre-synaptic cell stopped firing, its synaptic input would decay sufficiently to allow the post-synaptic cell to fire. In this scenario, the firing patterns of each cell would have a much wider spread of ISIs. In order to calculate $L = F(h^*)$ in this case, we have to keep track of the time required for the nullcline of the bursting cell to cross the lower branch of the w-nullcline (i.e. time to the saddle-node bifurcation). In addition, we would then have to calculate the extra time that the post-synaptic neuron needs to reach v_h.

Another simplifying assumption of our model was that individual synaptic inputs are sufficient to force the inhibited cell below v_h. In many cases, however, summation of multiple IPSPs is necessary to produce effective inhibition of the postsynaptic neuron. We examined one such example in Fig. 10 by lowering v_h and using faster synaptic decay. The result was the appearance of discontinuities in the map G. A full analysis of this case requires keeping track of synaptic summation to find the time interval between the first spike in the burst and the time that the opposite inhibited neuron falls below v_h. Such an analysis, as mentioned earlier, would require construction of G as a feed-forward map so that the effect inter-spike intervals have on the summation of IPSPs can be taken into account. Although we did not address this issue in detail, the map G constructed for Fig. 10 shows the feasibility of constructing the one-dimensional map in this case.

A similar technique can be used to keep track of any influence of short-term synaptic dynamics such as facilitation and depression on the shape of the map G. Thus, the effect of short-term synaptic dynamics can be accounted for by the one-dimensional maps so long as these effects are short lived on the time scale of a burst and do not accumulate from burst to burst. Note that the presence of synaptic facilitation would possibly act synergistically with the T-current in producing bursting oscillations by increasing the duration and effectiveness of inhibition and therefore allowing for additional de-inactivation of the T-current. However, the analysis of this synergistic interaction requires only modifications in the map G because the map F is not strongly influenced by modifications of synaptic dynamics.

Note finally that we have only considered the case of identical cells. However, the method readily generalizes to the heterogeneous case, in which case the map can be written as $\mathcal{P}(L) = F_2(G_2(F_1(G_1(L))))$, where the subscript indicates the cell number corresponding to each of the single-cell maps. The analysis of the dynamics of a heterogeneous network is beyond the scope of the current work and will be explored in future studies.

4.4 Analysis of more complicated dynamics and complex systems

The one-dimensional map based approach can be applied to understand some of the more complicated dynamics of the two-cell network. For example, simple cobwebbing using the map (Fig. 9) revealed the existence of chaotic solutions which were then numerically obtained. The existence of higher order periodics can also be explored in this way. In a network consisting of a larger number of cells, the formulation of a one-dimensional map may be considerably more difficult. However, if the ISI remains a quantity of interest, then presumably the map can be built as the composition of several (more than two) single-cell maps, each of which measures a quantity of specific interest over some portion of the trajectory.

4.5 Conclusions

We have described a simple analytical tool, a one-dimensional map constructed from single-cell properties, for the analysis of the output of a relatively complex network model. This one-dimensional map accurately predicted the existence and stability of solutions to the network model as well as the presence of chaotic solutions and the simultaneous stability of multiple solutions. The one-dimensional map was built

by focusing on a subset of solutions of interest, i.e. anti-phase bursts, and using some basic simplifying assumptions. We emphasize that the usefulness of the one-dimensional map is primarily as an aid to understanding the behavior of the full model network. As such, the map is not meant as a substitute for the full model in producing and predicting outputs of the biological network of interest. Rather, a thorough understanding of biological neural networks would require a combination of numerical simulations using detailed biophysical models and the mathematical analysis of these high-dimensional models using reduction techniques such as the one described in this study.

Appendix

1 Model equations and parameters

The Morris–Lecar parameters in Eq. (6) are adapted from Keener and Sneyd (1998):

$I_{app} = 14\mu\text{A/cm}^2$, $C_m = 2\mu\text{F/cm}^2$, $\phi = 2/3$, $E_K = -84$, $E_{Ca} = 120$, $E_L = -60$, $g_{Ca} = 4$, $g_K = 8$, $g_L = 2$. Here the voltage units are mV, and conductance units are mS/cm^2.

The functions m_∞, w_∞ and $\tau_w(v)$ are given by

$$m_\infty(v) = \frac{1 + \tanh[(v + 12)/18]}{2},$$

$$w_\infty(v) = \frac{1 + \tanh[(v + 8)/6]}{2},$$

$$\tau_w(v) = \frac{1}{\cosh[(v + 8)/12]} \tag{17}$$

The discontinuous dynamics of $h_j(t)$ and $s_j(t)$ in Eqs. (3), (4) and (6) are smoothed out in the numerical simulation using:

$$a_j = \sigma(v_j - v_h)$$

$$h'_j = \sigma(v_h - v_j) \frac{1 - h_j}{\tau_{lo}} - \sigma(v_j - v_h) \frac{h_j}{\tau_{hi}}$$

$$s'_j = \sigma(v_j - v_\theta) \frac{1 - s_j}{\tau_\gamma} - \sigma(v_\theta - v_j) \frac{s_j}{\tau_{syn}}$$

where $\sigma(v)$ is the sigmoidal function given by

$$\sigma(v) = \frac{1}{2}[1 + \tanh(4v)]$$

The T-current inactivation time is set to $\tau_{hi} = 20$ ms, while the synaptic growth time is $\tau_\gamma = 0.2$ ms. The synaptic reversal potential is set to $E_{inh} = -80$ mV.

Except for the figure panels exploring the parameter sensitivity of the network dynamics, the remaining parameter values in Figs. 2–9 are: $v_h = -47.5$ mV, $\tau_{lo} = 200$ ms, $\bar{g}_{syn} = 0.6$ mS/cm^2, $\bar{g}_T = 1$ mS/cm^2, $v_\theta = -35$ mV, and $\tau_{syn} = 4$ ms.

In Fig. 1, 10 and 11, these parameters are changed to: $v_h = -52$ mV, $\tau_{lo} = 100$ ms, $\bar{g}_{syn} = 1.1$ mS/cm^2, $\bar{g}_T = 1.4$ mS/cm^2, $v_\theta = -3$ mV, and $\tau_{syn} = 1$ ms.

The values of τ_{hi} and τ_{lo} given above are close to the values measured by Huguenard and McCormick (1992) of about 30 ms and 300 ms, respectively.

MATLAB code implementing the model can be found at http://web.njit.edu/~matveev/Burst.

Note that in principle the precise value of v_θ is not critical to the model dynamics, provided that v_θ is less than the maximal potential of the spiking limit cycle. However, a more hyperpolarized level of v_θ used in Figs. 2–9 allows for a more reliable inhibition by the cell initiating the burst, ensuring that the potential of the cell terminating the burst quickly drops below v_h. On the other hand, the use of a higher spiking threshold enhances the situation whereby a single burst spike is insufficient to suppress the potential of the partner cell below v_h, a situation which holds in the case of multistability of solutions (Figs. 1, 10 and 11). However, the same effect could be achieved by varying $\bar{g}_{syn}$ alone.

Finally, in the computation of the single-cell map $L = F(h^\star)$, we ignored a minor contribution to the burst length of the duration between cell escape time and the peak of first spike. This correction is easy to include, and is incorporated in all numerical calculations involving this map. Denoting the time to first spike as $\Delta t(h^\star)$, the sums in Eqs. (10–12) should be extended to include $\Delta t(h^\star)$, and in Eq. (9), h_1 should be set to $h^\star \exp[-\Delta t(h^\star)/\tau_{hi}]$.

2 Numerical reconstruction of burst bifurcation diagram

The phase diagrams shown in Fig. 8 (gray curve) and in 11 are reconstructed numerically, by "crawling" along the relevant parameter direction. The algorithm is implemented in MATLAB, and involves two main parts: (1) the periodic state detector, and (2) the parameter "crawler"/continuer.

1. The detector of periodic solutions is implemented in the most straightforward way. Namely, model equations are continuously integrated while checking for a pattern in the sequence of burst intervals.

A burst interval is defined as the time period between two consecutive spikes of one cell containing at least one spike of the second cell. If a sequence of such intervals is found to repeat itself a sufficient number of times with a given degree of accuracy, the corresponding state is assumed periodic, and the number of spikes, the duration of the state and its state vector are returned. For a symmetric anti-phase periodic bursting solution, the burst interval sequence would normally represent the lengths of consecutive bursts of the two cells, such as in { 35.4, 35.4, 35.4, ...}. However, in some cases the synchronization of the last and first spikes in the burst may occur, which may lead to a periodic sequence of length 4, such as { 25.2, 2.1, 1.4, 25.2, 2.1, 1.4, 25.2, 2.1, 1.4 }. The latter sequence corresponds to the situation where the last spike of one cell occurs after the first spike of the partner cell. In this example 1.4 represents the first intra-burst inter-spike interval (containing one last spike of the partner cell), and 2.1 is the duration of the last inter-spike interval of the partner cell (containing one first spike of cell 1). However, this complication does not arise in the simulations shown in this work. Empirically, tracking the lengths of burst intervals defined above is more robust than tracking the sequence of the inter-spike intervals. Also, it automatically takes into account the identity of the spikes as coming from a particular cell.

2. Once a periodic solution is detected, a variation of a standard predictor-corrector step is performed. Namely, the relevant parameter is increased by a certain increment (or decreased, depending on the direction of the crawl), and the periodic detection is repeated, using the periodic state from the preceding parameter point as the initial condition. If the new periodic solution has the same number of spikes (burst sequence signature) as for a previous parameter value, a bigger parameter step is undertaken (parameter increment is stretched). If the new periodic state is different from the old one, the parameter increment is decreased, and the new state sequence is put into a queue along with the corresponding parameter value and the full state vector. The process continues until the parameter step drops below a certain minimal value, which will occur close to the boundary (bifurcation point) of the parameter interval supporting the corresponding periodic state.

Once one boundary of the relevant parameter interval is detected, the crawl is re-started from the initial parameter point, but in the opposite direction (i.e. the parameter is decreased). When the

second parameter bound/bifurcation is detected, the parameter basin of the stable state has been determined. The process is then repeated for the next periodic state in the parameter queue. Recall that the queue is composed of activity states that the algorithm encounters when the parameter value is increased beyond the bifurcation point. Therefore, the algorithm "hops" from one state to another one which lies close to the first one in the parameter space.

Note that the completeness of the reconstructed phase diagram is by no means guaranteed. For instance, if the parameter support of one state lies completely within the parameter state of the other cell, that state may never be detected, unless it lies close to the bifurcation point of some third stable periodic state.

3 Case of discontinuous $h^\star = g(L)$ map

Here we describe the reconstruction of the discontinuous $h^\star = g(L)$ map shown in Fig. 10(b). The discontinuity is directly related to the amount of time needed for the cell potential to drop below the v_h threshold after burst termination. This time duration is labeled ϕ and marked by a double arrow in Fig. 10(a). If the T-current threshold v_h is close to the spiking threshold of the cell, as is the case for the simulations in Figs. 2–9, the potential of each cell will reach v_h almost instantaneously on burst termination, and ϕ is approximately zero (ϕ is ignored in Eqs. (13–15)). If however v_h is significantly lower than the potential of the cell upon burst termination, it may take several inhibitory synaptic inputs to lower the potential below v_h.

ϕ depends on the level of T-current inactivation of both cells, $\phi = \phi(h^\star, h_L)$, where h_L is the T-current inactivation of the bursting cell at the end of the burst (see Fig. 10(a)). The larger h_L, the higher is the V-nullcline of the cell on termination of its burst, and the longer it takes for the potential of the cell to drop below the v_h threshold. ϕ is also a function of $h^\star$, since $h^\star$ determines the initial burst spiking frequency, and hence, it determines how quickly the inhibitory synaptic input can lower the potential of the suppressed cell below v_h.

Thus, the de-inactivation of the T-current is described by

$$h^* = 1 + (h_o - 1)\exp\left[-\frac{L - \phi(h^\star, h_L)}{\tau_{lo}}\right]$$

where h_o (the minimal value of $h(t)$) and h_L are determined using the steady-state approximation, i.e. under the assumption of periodicity in burst characteristics $h^\star$, ϕ and L. Examination of Fig. 10(a) leads to:

$$h_o = h^* \exp\left[-\frac{L + \phi(h^\star, h_L)}{\tau_{hi}}\right]$$

$h_L = h^* \exp\left[-\frac{L}{\tau_{hi}}\right]$ Thus, ϕ is a function of both $h^\star$ and L:

$$\phi(h^\star, h_L) = \phi(h^\star, h^* \exp[-L/\tau_{hi}]) \equiv \Phi(h^\star, L)$$

Therefore, we have

$$h^\star = 1 + \left(h^* \exp\left[-\frac{L + \Phi(h^\star, L)}{\tau_{hi}}\right] - 1\right)$$
$$\exp\left[-\frac{L - \Phi(h^\star, L)}{\tau_{lo}}\right]$$

Solving for $h^\star$ yields

$$h^\star = \frac{1 - \exp\left[-\frac{L - \Phi(h^\star, L)}{\tau_{lo}}\right]}{1 - \exp\left[-\frac{L + \Phi(h^\star, L)}{\tau_{hi}} - \frac{L - \Phi(h^\star, h_L)}{\tau_{lo}}\right]} \equiv H(h^\star, L)$$

(18)

In the above equation, the function $\Phi(h^\star, L)$ is defined numerically. Namely, the potential of one cell (bursting cell) is set above the spiking threshold, while the potential of the partner cell (the suppressed cell) is set below the excitation threshold, and their h values are set respectively to $h^\star$ and $h_L = h^* \exp[-L/\tau_{hi}]$. Given these initial conditions, the feedforward network equations are then integrated until the potential of the suppressed cell reaches v_h. The corresponding passage time determines the value $\phi(h^\star, h_L)$.

Since the right-hand side of Eq. (18) depends on $h^\star$ through $\Phi(h^\star, L)$, this equation defines the $h^\star = G(L)$ map implicitly. It is solved iteratively for each value of L:

$$h^\star_{n+1} = H(h^\star_n, L), \quad n = 1, 2, ...$$

where the initial condition $h^\star_1$ is obtained under the approximation $h_o = 0$, $\phi = 0$:

$$h^\star_1 = 1 - \exp\left[-L/\tau_{lo}\right]$$

The iterative solution approaches the thin curve shown in Fig. 10(a). The discontinuity in this curve is the result of the discontinuity of the function $\phi(h^\star, h_L)$: as $h^\star$ decreases or h_L increases past some critical value, it will take one more inhibitory input to suppress the cell below v_h, resulting in a jump increase in ϕ by one inter-spike interval.

References

Bartos, M., Manor, Y., Nadim, F., Marder, E., & Nusbaum, M. P. (1999). Coordination of fast and slow rhythmic neuronal circuits. *Journal of Neuroscience, 19,* 6650–6660.

Bertram, R., & Sherman, A. (2000). Dynamical complexity and temporal plasticity in pancreatic beta-cells. *Journal of Biosciences, 25,* 197–209.

Bose, A., Manor, Y., & Nadim, F. (2001). Bistable oscillations arising from synaptic depression. *SIAM Journal on Applied Mathematics, 62,* 706–727.

Butera, R. J. (1998). Multirhythmic bursting. *Chaos, 8,* 274–284.

Canavier, C. C., Baxter, D. A., Clark, J. W., & Byrne, J. H. (1994). Multiple modes of activity in a model neuron suggest a novel mechanism for the effects of neuromodulators. *Journal of Neurophysiology, 72,* 872–882.

Canavier, C. C., Clark, J. W., & Byrne, J. H. (1991). Simulation of the bursting activity of neuron R15 in Aplysia: Role of ionic currents, calcium balance, and modulatory transmitters. *Journal of Neurophysiology, 66,* 2107–2124.

Chay, T. R., & Rinzel, J. (1985). Bursting, beating, and chaos in an excitable membrane model. *Biophysical Journal, 47,* 357–366.

Coombes, C., & Bressloff, P. (Eds.) (2005). *Bursting: The genesis of rhythm in the nervous system.* London: World Scientific.

Destexhe, A., & Sejnowski, T. J. (2003). Interactions between membrane conductances underlying thalamocortical slow-wave oscillations. *Physiological Reviews, 83,* 1401–1453.

Ermentrout, G. B., & Kopell, N. (1998). Fine structure of neural spiking and synchronization in the presence of conduction delays. In *Proceedings of the National Academy of Sciences of the United States of America, 95,* 1259–1264.

Grillner, S., Markram, H., De Schutter, E., Silberberg, G., & LeBeau, F. E. (2005). Microcircuits in action—from CPGs to neocortex. *Trends in Neurosciences, 28,* 525–33.

Hines, M., Morse, T., Carnevale, N., & Shepard, G. (2004). Model DB: A database to support computational neuroscience. *Journal of Computational Neuroscience, 17,* 7–11.

Huguenard, J. R. (1996). Low-threshold calcium currents in central nervous system neurons. *Annual Review of Physiology, 58,* 329–48.

Huguenard, J. R., & McCormick, D. A. (1992). Simulation of the currents involved in rhythmic oscillations in thalamic relay neurons. *Journal of Neurophysiology, 68,* 1373–1383.

Izhikevich, E. M., & Hoppensteadt, F. C. (2004). Classification of bursting mappings. *International Journal of Bifurcation and Chaos, 14,* 3847–3854.

Keener, J., & Sneyd, J. (1998). *Mathematical physiology* (pp. 154–155). New York: Springer-Verlag.

Lechner, H. A., Baxter, D. A., Clark, J. W., & Byrne, J. H. (1996). Bistability and its regulation by serotonin in the endogenously bursting neuron R15 in Aplysia. *Journal of Neurophysiology, 75,* 957–962.

Lee, E., & Terman, D. (1999). Uniqueness and stability of periodic bursting solutions. *Journal of Difference Equations, 158,* 48–78.

Lofaro, T., & Kopell, N. (1999). Timing regulation in a network reduced from voltage-gated equations to a one-dimensional map. *Journal of Mathematical Biology, 38,* 479–533.

Llinas, R. R., & Steriade, M. (2006). Bursting of thalamic neurons and states of vigilance. *Journal of Neurophysiology, 95,* 3297–3308.

Manor, Y., & Nadim, F. (2001). Synaptic depression mediates bistability in neuronal networks with recurrent inhibitory connectivity. *Journal of Neuroscience, 21,* 9460–9470.

Marder, E., & Calabrese, R. (1996). Principles of rhythmic motor pattern generation. *Physiological Reviews, 76,* 687–717.

Masino, M. A., & Calabrese, R. L. (2002). Period differences between segmental oscillators produce intersegmental phase differences in the leech heartbeat timing network. *Journal of Neurophysiology, 87,* 1603–1615.

Medvedev, G. (2005). Reduction of a model of an excitable cell to a one-dimensional map. *Physica D, 202,* 37–59.

Morris, C., & Lecar, H. (1981). Voltage oscillations in the barnacle giant muscle fiber. *Biophysical Journal, 35,* 193–213.

Perkel, D. H., & Mulloney, B. (1974). Motor pattern production in reciprocally inhibitory neurons exhibiting postinhibitory rebound. *Science, 185,* 181–183.

Rubin, J., & Terman, D. (2000). Geometric analysis of population rhythms in synaptically coupled neuronal networks. *Neural Computation, 12,* 597–645.

Satterlie, R. (1985). Reciprocal inhibition and postinhibitory rebound produce reverberation in a locomotor pattern generator. *Science, 229,* 402–404.

Selverston, A., & Moulins, M. (1986). *The Crustacean stomatogastric system : A model for the study of central nervous systems.* Berlin Heidelberg New York: Springer.

Skinner, F. K., Kopell, N., & Marder, E. (1994). Mechanisms for oscillation and frequency control in reciprocally inhibitory model neural networks. *Journal of Computational Neuroscience, 1,* 69–87.

Sohal, V., & Huguenard, J. (2001). It takes T to tango. *Neuron, 31,* 35–45.

Terman, D. (1994). Chaotic spikes arising from a model of bursting in excitable membranes. *SIAM Journal on Applied Mathematics, 51,* 1418–1450.

Terman, D., Kopell, N., & Bose, A. (1998). Dynamics of two mutually coupled slow inhibitory neurons. *Physica D, 117,* 241–275.

Traub, R. D., Whittington, M. A., Colling, S. B., Buzsaki, G., & Jefferys, J. G. (1996). Analysis of gamma rhythms in the rat hippocampus in vitro and in vivo. *Journal of Physiology, 493,* 471–484.

Van Vreeswijk, C., Abbott, L. F., & Ermentrout, B. (1994). When inhibition not excitation synchronizes neural firing. *Journal of Computational Neuroscience, 1,* 313–321.

Wang, X. J., & Buzsaki, G. (1996). Gamma oscillation by synaptic inhibition in a hippocampal interneuronal network model. *Journal of Neuroscience, 16,* 6402–6413

Wang, X. J., & Rinzel, J. (1992). Alternating and synchronous rhythms in reciprocally inhibitory model neurons. *Neural Computation, 4,* 84–97.

Wang, X. J., & Rinzel, J. (1994). Spindle rhythmicity in the reticularis thalami nucleus: Synchronization among mutually inhibitory neurons. *Neuroscience, 53,* 899–904.